Proceedings of the Canadian Society for Mechanical Engineering International Congress 2021
CSME Congress 2021
June 27-30, 2021, Charlottetown, PE, Canada

Benchmark physical and mechanical property chararacterization of 316L stainless steel DMLS prints

Lucas Gallant[1], Amy Hsiao, Grant McSorley
Faculty of Sustainable Design Engineering, University of Prince Edward Island, Charlottetown, Canada
*lggallant@upei.ca

Abstract—Industrial acceptance of metal additive manufacturing (AM) is continuously rising along with its rapid development. As such, continuous research is needed to better understand the process and print characteristics to control and improve process parameters and as-built part quality. Dimensional tolerance, surface characteristics, and mechanical properties are all key qualities to assess for printer performance enhancement and repeatability. This paper presents results for physical and mechanical property inspections and testing on a designed test artifact for the benchmarking of 3D metal printers. The properties investigated include tensile strength, hardness, dimensional accuracy, roughness, and dross formation on overhanging features. Printed artifact results show similar anisotropic mechanical properties, with tensile strengths within the manufacturer-rated ranges. Dimensional XY-plane tolerances were within -0.18 to 0.18 mm and Z-axis tolerance within -0.10 to 0.10 mm for both printers. As-built roughness values were below manufacturer maximums for both Ra and Rz. The overhang performance was similar for both machines, with increasing dross for decreasing overhang angles.

Keywords-DMLS; benchmark; additive manufacturing; mechnaical properties; accuracy; roughness; overhangs

I. INTRODUCTION

Industrial acceptance of additive manufacturing (AM) is continuously rising along with its rapid development. As such, direct metal laser sintering (DMLS) technology has established itself as a fabrication technique in numerous industries, especially aerospace, tooling, automotive, and medical applications [1]. Although the use of DMLS is becoming established, further implementation is slowed by matters of part accuracy, surface properties, and control of mechanical properties [2]. There is a lack of standards for AM and DMLS such that benchmarking is necessary to gain information about specific machine capabilities and print quality, especially with the increase of available metal printing solutions to be used in industrial settings [3]. This paper focuses on presenting results of printing a designed test artifact with features for the characterization of tensile strength, hardness, dimensional analysis, roughness, and overhang printability on EOS M100 and EOS M290 printers using stainless steel (SS) 316L powder.

II. BENCHMARKING

An in-depth review for the design of the novel AM test artifact used in this study has been reported in a previous work [4]. The design followed 'rules' for ideal AM test part design outlined by Moylan, Ritcher and Jacobs, and Scarvetti [2, 5, 6]. Though the design took influence from many benchmark parts, the final test artifact is largely a modified design of the proposed standard test artifact by Moylan. It was necessary to make the modifications to allow for as-built mechanical properties to be tested with available machines, as well as other build properties such as residual stress. The new artifact was also specified to fit the build volume of the EOS M100 printer produced by EOS GmbH (build volume of Ø100 x 95 mm). Additionally, a cone volume support pattern was developed for the outer edges of the part to prevent the corners from lifting due to thermal stresses. This study focuses on the mechanical and physical observations taken from the designed part.

III. METHODOLOGY

A. Test Artifact Features

The model for the new test artifact is shown in Fig. 1. The design includes many features designed for physical and mechanical investigation. Features that are focused on for this paper are the vertical and horizontal tensile specimens (8, 9), the flat surfaces (3, 10), all straight, angled, and circular overhangs (1, 5, 11), all small features (2, 6), as well as other holes and bosses used for dimensional accuracy (7, 14). All noted features and their corresponding inspection tools can be seen in Table 1.

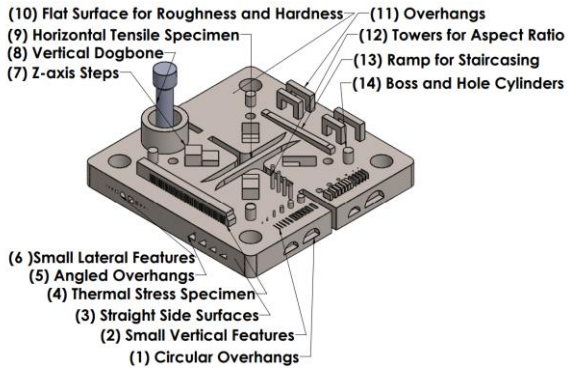

Figure 1. New test specimen design with feature labels.

TABLE I. TABLE OF TEST ARTIFACT FEATURE TYPES, DIMENSIONS, AND CORRESPONDING CHARACTERIZATION TOOLS

Feature No.	Type of Feature	Dimensions	Inspection Method
1	Circular overhangs	5 – 8 mm diameter	ISM Digital Analyzer
2	Small vertical features	0.1 – 2 mm	ISM Digital Analyzer
3	Straight side surfaces	70 mm	Calipers, indicator
5	Angled overhangs	30 – 45 degrees	ISM Digital Analyzer
6	Small lateral features	0.1 – 2 mm	ISM Digital Analyzer
7	Z-axis steps	2 mm	Height gauge
8	Vertical dog bone	5 mm diameter	TQ SM1002 Bench Top Tensile Testing Machine
9	Horizontal tensile specimen	2 mm x 8 mm	TQ SM1002
10	Flat surface for roughness and hardness	n/a	Starett SR100 Surface Roughness Tester, TQ SM1002, and ISM Digital Analyzer
11	Overhangs	4 – 7 mm	ISM Digital Analyzer
14	Boss and hole cylinders	3 mm diameter	Calipers

B. *Feature Characterization*

1) Tensile Specimens: The test artifact includes two specimens for tensile strength testing. One of the specimens is printed vertically and the other horizontally as it has been shown that the build direction of parts printed through DMLS processes impacts their strength properties greatly [7]. The specimens will identify how these variations may be different between machines. The first specimen is a round dog bone (5 mm diameter) in the z-axis designed to be tested on a TQ SM1002 Bench Top Tensile Testing Machine. The second specimen is a plate-type dog bone, which is part of the test artifact base itself in the x-y plane; the specimen has a nominal cross section of 2 mm x 8 mm with 10 mm corner radii. The horizontal specimen was designed as part of the main body of the test artifact part for spatial efficiency, and it also allows for direct measurement of the test artifact strength as it will conduct thermal energy through the artifact; this tensile testing requires a custom gripper to ensure axial loading of the applied force. Both specimens are tested as built to simulate the mechanical behaviour of a part printed with minimal post-processing, so to include any effects from the surface quality.

2) Hardness: Designated areas are defined on both the top and side surfaces of the test specimen for Brinell hardness testing following ASTM E10 [8]. The top surface area used is noted in Fig. 1 and allows for three indents to be made with sufficient spacing (3 x diameter). The side indents were made near the circular overhangs. Indent surfaces were ground using 120-grit abrasive paper before the indents were taken to reduce optical measurement error from the rough surfaces. Brinell Hardness (HB) values from the indents on each surface were taken and aveeraged for comparisons. Using a TQ SM1002 Bench Top Tensile Testing Machine and a digital microscope, the diameter of the indentation resulting from a 1500 kgf load from a 10-mm steel indenter is measured.

3) Roughness: The test artifact included specified areas on both the top surface and the sides for arithmetical mean deviation (Ra) and maximum peak to valley height (Rz) roughness measurements to be taken using a Starett SR100 Surface Roughness Tester. A series of 3 measurements are taken and averaged for specified directions on the top and side surface areas.

4) Dimensional Accuracy: Two methods of characterizing dimensional capabilities of the printers are considered: minimum feature size and overall accuracy of dimensional features. The minimum feature size is assessed by a qualitative observation of the print success for vertical rectangular and circular bosses and holes, and lateral square and circular holes; the features are either considered failed when there is no formation of the hole or boss, partial if there is incomplete formation, or successfully printed otherwise. Overall accuracy is determined by considering the dimensional error of boss and hole features, the step features, and the artifact itself. Maximum and minimum error make up the tolerance range for the printers.

5) Overhangs: Three different unsupported overhanging features are assessed by the test artifact: straight overhangs, circular overhangs, and angled overhangs. All three overhang types require different evaluation measures to quantify their print success and dross defects simply.

Four unsupported straight overhang bridges were included in the test artifact at lengths from 4-7 mm to test the limits of unsupported overhangs. Though there is observed overheating and burning, the surface morphology of the straight overhangs is dominated by the dross formation and sagging. Dross formation in metal AM is primarily due to the sintering of supporting powder as the heat dissipation through the powder is restricted, providing lower conductivity than support structures. The lower conductivity results in more energy absorbed and thus a larger melt pool, which sinks due to gravity and capillary forces. The related sagging occurs when there is insufficient support for the large melt structure [9, 10]. As such, this accumulation is characterized by it's 2D area. The area of the addtitonal dross is determined by taking 5

equally spaced measurents of the bridge thickness with an digital microscope; the area can then be calculated using the Midpoint Rule. The error of the bridge area from the CAD model can then be calculated to find what will be labelled as dross area error (DAE). Fig. 2 shows an example of the dross formation observed.

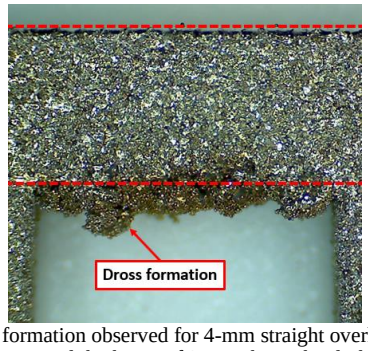

Figure 2. Dross formation observed for 4-mm straight overhang (M100_1), with the nominal thickness of 2 mm shown by dashed lines.

The circular overhangs are characterized by the theoretical eccentricity of the half-circle. Eccentricity has been used to characterized metal powder bed fusion features [11, 12]. For the lateral arc overhangs, eccentricity is essentially being used as a measure of the extent to which the rough dross defects of unsupported arcs impact the circular geometry. A measurement is taken of for the major axis (the base length, d_M) and the minor axis (the maximum arc height, r_m). The resulting eccentricity, e, is calculated.

$$e=\sqrt{1-(2r_m)^2/d_M^2} \quad (1)$$

The dross on the angle overhangs is characterized by the error of the height dimension (opposite the orientation angle) measured by the digital microscope.

IV. Results & Discussion

A combined total of 12 test artifacts were printed on the M100 and M290 using CT PowderRange 316L and EOS StainlessSteel 316L powders, respectively [13, 14]. The metal powders used have similar compositions and average powder sizes. Two print jobs were completed on the M290 printer, with four artifacts in each run. The four artifacts were printed in two different orientations, 180 degrees from each other; a print layout on the build platform can be seen in Fig. 3. The orientations on the second M290 print were rotated 180 degrees from the first print. The remaining four artifacts were printed individually on the M100, also at 0 and 180-degree orientations.

All print jobs were run using default parameters for each machine. A comparison of the printers for machine specifications and energy density of the default stripes skin exposure parameters is seen in Table 2. The M100 printer has a smaller build volume and baseplate, a lower-power laser, a smaller laser focus diameter, and a smaller default layer thickness. The M100 has a higher volume energy density (VED), calculated using power (P), scan velocity (v) hatch distance (h_d), and layer thickness (t):

$$VED=\frac{P}{v\cdot h_d\cdot t} \quad (2)$$

TABLE II. Table of Differences Between EOS DMLS Printers

Machine Spec.	EOS M100	EOS M290
Build Volume	Ø 100 x 95 mm	250 x 250 x 325 mm
Laser Type	200 W Yb fibre laser	400 W Yb fibre laser
Focus Diameter	40 µm	100 µm
Layer Thickness	20 µm	40 µm
Default VED	66.6 J/mm^3	57.7 J/mm^3

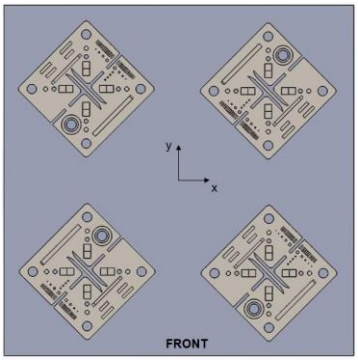

Figure 3. Top view drawing of the M290 test artifact build layout, with the x-axis denoting the direction of the recoating blade.

A. *Tensile Strength*

The means of tensile strength for the two machines and two specimen orientations is found in Table 3. The resulting interval plot can be found in Fig. 4.

TABLE III. Table of Tensile Strength Results

Printer	Build Orientation	Tensile Strength (MPa) ± SD
M100	Horizontal	639 ± 15
M100	Vertical	581 ± 6
M290	Horizontal	662 ± 15
M290	Vertical	590 ± 11

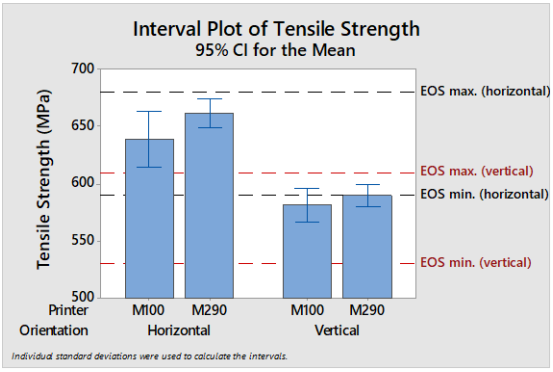

Figure 4. Interval plot for the tensile strength of as-built horizontal and vertical tensile specimens

Conducting t-tests on the data using Minitab software reveals that both M100 and M290 printers show statistically significant differences between the vertical and horizontal strengths (p=0.002 and p=0.000, respectively), with the stronger being the horizontal. As such, tensile strength is observed to be an anisotropic mechanical property for the DMLS process in both machines. This is in line with expected results and results from the literature [7, 15], as the tensile load for the vertical dog bone is perpendicular to the layering of the printed part, therefore increasing the risk of failure.

It can also be seen that there is no statistically significant difference between the printers themselves. As well, all of the data points for the two printers fall within the respective maximum and minimum ranges specified by EOS [14].

B. Hardness

The means of the sample data from the two machines and two indent surfaces is found in Table 4. The resulting interval plot can be found in Fig. 5.

TABLE IV. TABLE OF SURFACE HARDNESS RESULTS

Printer	Surface	HB 10/1500 ± SD
M100	Side	194 ± 3
M100	Top	206 ± 1
M290	Side	189 ± 3
M290	Top	203 ± 3

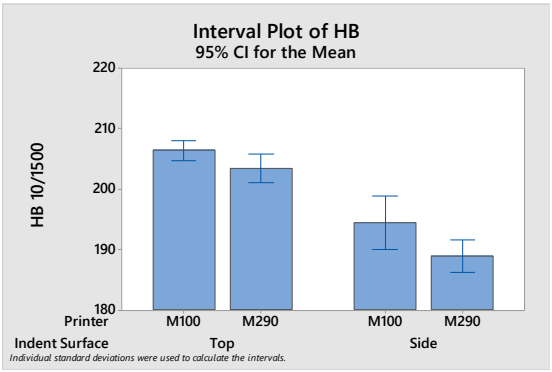

Figure 5. Interval plot for the hardness of top and side artifact surfaces.

Conducting t-tests on the data reveals that both M100 and M290 printers show statistically significant differences between the top and side hardnesses (p=0.004 and p=0.000, respectively), with the harder surface being the top. As such, macro-hardness is observed to be an anisotropic mechanical property. This agrees with hardness anisotropy in the literature [16].

C. Roughness

The results from the stylus profilometer testing can be found in Table 5 and Fig. 6. T-test results show no difference between printers or surfaces for Ra or Rz. It is often observed that the side roughness of parts can be lower than the top roughness [17]. All the data falls under the maximum roughness values given by EOS [14].

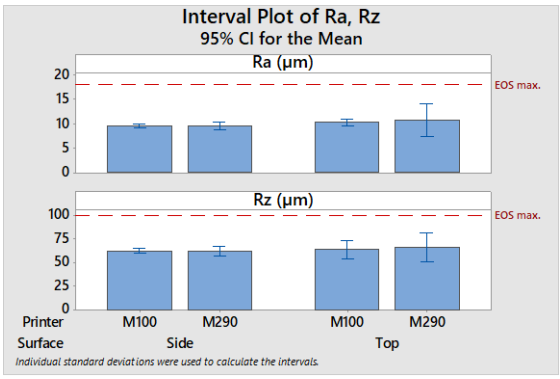

Figure 6. Interval plot for the roughness of as-built top and side surfaces.

TABLE V. TABLE OF SURFACE ROUGHNESS RESULTS

Printer	Surface	Ra (um) ± SD	Rz (um) ± SD
M100	Side	9.5 ± 0.3	63.1 ± 1.8
M100	Top	10.2 ± 0.4	64.4 ± 5.9
M290	Side	9.5 ± 1.0	62.8 ± 6.3
M290	Top	10.7 ± 4.1	66.9 ± 18.9

D. Dimensional Accuracy

The M290 printer appears to have a wider tolerance range than the M100, with an XY dimensional error from -0.10 to 0.10 mm and Z error of -0.18 to 0.18 mm, compared to the -0.04 to 0.06 mm (XY) and -0.13 to 0.09 mm (Z) max. and min. error with the M100. For the Z-planes, this difference may be attributed to the difference in layer height of the two default parameter sets. Additionally, the ranges for the XY-plane tolerances appear to be narrower than the Z-planes for both machines.

Observations from the set of prints suggest that the resolution capabilities of the printers in the XY plane varies depending on whether the part is a boss or a hole, with the M100 more capable for the creation of small hole features, while the M290 is more capable in the creation of small bosses (Fig. 7). Table 6 categorizes small feature success based on observation with a digital microscope. A feature is considered to be failed (F) if there is no formation for the bosses and if there are no open gaps for the holes, partial (P) if there is an incomplete formation for the bosses and if the hole is mostly closed off for holes, and otherwise is considered to have successfully printed (S). Fig. 8 provides a labelled CAD visual of the small vertical features.

For lateral features, the 250-micron in features were compared in Table 6, as all 100-micron features failed. In the case that the two sides of the test artifact had different print success, the better printed holes were listed. There does not appear to be a clear difference between the performance of the printers.

TABLE VI. TABLE OF SMALL FEATURE PRINT SUCCESS

Feature (100 µm)	M100				M290							
	1	*2*	*3*	*4*	*1*	*2*	*3*	*4*	*5*	*6*	*7*	*8*
Rectangular boss	F[a]	F	F	F	P[b]	F	F	F	P	P	P	F
Rectangular walls	F	F	F	F	P	S[c]	S	F	S	P	F	F
Rectangular hole	P	S	P	P	F	F	F	F	F	P	F	F
Rectangular spaces	S	S	S	S	P	P	P	P	P	P	P	P
Circular boss	F	F	F	F	S	S	S	S	S	S	S	S
Circular hole	P	P	P	P	F	F	F	F	F	F	F	F
Lateral squares (250 µm)	F	P	P	P	F	P	P	P	P	P	F	P
Lateral circles (250 µm)	P	P	P	P	P	P	P	P	F	P	P	P

a. Fail b. Partial c. Success

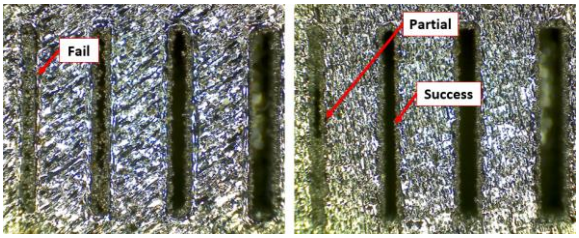

Figure 7. Labelled success of small rectangular holes for M290_1 (left) and M100_1 (right) taken with ISM Digital Analyzer

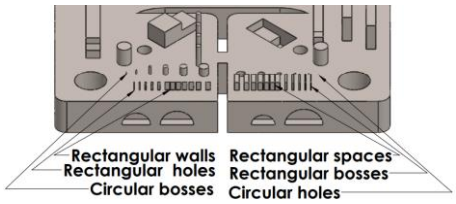

Figure 8. Small vertical features of the test artifact

E. *Overhanging Features*

1) Straight Overhangs: The resulting mean dross area errors can be seen in Fig. 9. A one-way ANOVA test was used to test for any significant difference between the DAE of the overhang lengths; Levene's test for equal variances was used to confirm the assumption of equal variances for the ANOVA. The tests yielded that there is no statistical difference betweeen any of the overhang lengths ($F(3,44) = 1.36$, $p = 0.269$). As such, the data of from difference overhang lengths were grouped to compare the DAE of the two printers through a 2-sample t-test. The t-test showed that there is no statistical difference in DAE between the M100 and M290 printers.

General recommendations in the literature advise that unsupported overhangs not exceed around 2 mm [18]. The lack of a definitive relationship betweeen the DAE and length may be due to the instability being too high at such long unsupported bridge lengths.

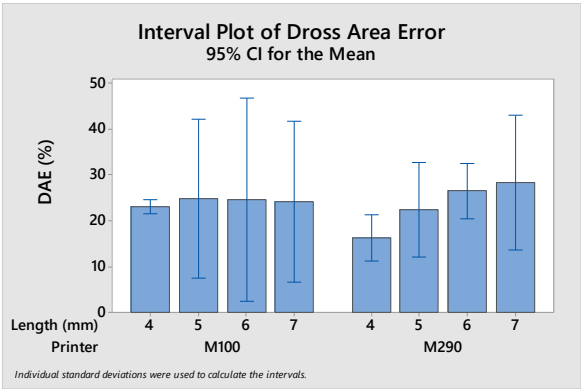

Figure 9. Interval plot for the dross area error of the straight overhangs.

2) Circular Overhangs: The resulting mean eccentricities can be seen in Fig. 10. The lower the eccentricity, the more accurate the printed semi-circle is to the CAD model. There was a statistically significant difference between groups as determined by one-way ANOVA ($F(3,92) = 5.17$, $p = 0.002$). A post-hoc Tukey test was used to determine which specific groups differed. This multiple comparison test revealed that there are differences between the eccentricities from the 8 mm nominal diameter holes to 5 mm, and even 7 mm to 5 mm. The trend shows decreasing eccentricity for increasing diameter. This unintuitive result may be explained by the competing phenomena of burning and sagging (dross) for circular overhangs [10]. While sagging occurs from low conductivity forming large melt pools, burning occurs from insufficient dissipation of the subsequent heat energy. The sagging phenomena may be dominating at smaller arc diameters, but then be increasingly offset by burning effects as the diameters increase. This effect is shown in Fig. 11, as the 5-mm diameter overhang exhibits dross formation and potential sagging, whereas the 8-mm diameter overhang additionally exhibits incresed burning near the apex.

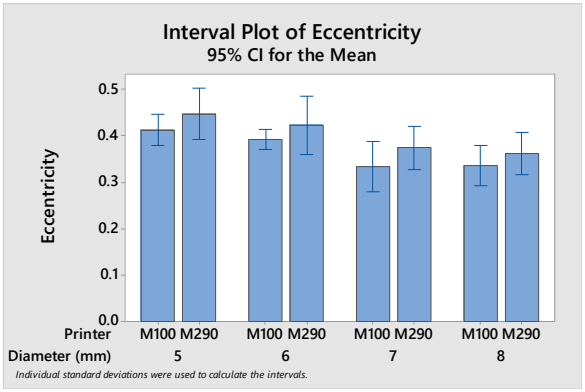

Figure 10. Interval plot for the dross area error of the straight overhangs.

Since the different arc diameters effect the resulting eccentricity, individual t-tests at each diameter were used to reveal that there is no significant difference in eccentricity of unsupported arcs between the two printers.

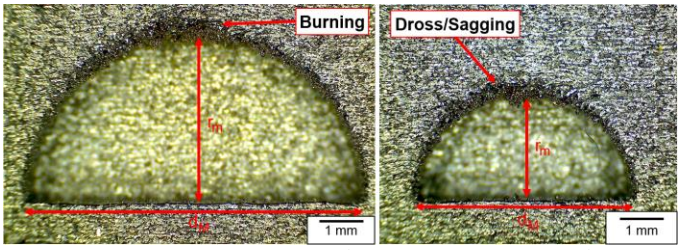

Figure 11. Digital microscope images of 5 mm (right) and 8 mm (left) circular overhangs from artifact M290_1, showing dross formation for on both surfaces and increased burning in the larger arc radius.

3) Angled Overhangs: The resulting mean errors for the angled overhangs can be seen in Fig. 12. A one-way ANOVA ($F(3, 92) = 17.74$, $p = 0.000$) with Levene's test for equal variances and a post-hoc Tukey test revealed that all overhang angles differed significantly in dimensional error at $p < 0.05$, with the exceptions of 45 to 40 degrees and 40 to 35 degrees. The trend from this test shows that the error (dross, surface roughness) increases with decreasing angles. This result alligns with the literature that angled overhangs begin to fail when unsupported at angles below 35 degrees [10, 19].

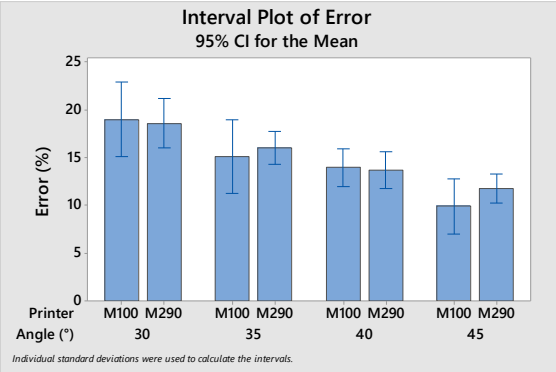

Figure 12. Interval plot for the height error of angled overhangs.

Individual t-tests at each angle reveal that there is no significant difference in error for unsupported angles between the two printers.

F. Next Steps

Though the printers exhibited similar print performance for the dimensional and mechanical features, there remains material property investigations to be completed for the printed artifacts to complete the benchmarking. Remaining inspections would include density and porosity, residual stress, and any microstructural characterization to be made.

Additionally, it would be informative to print the test artifact on the M100 using the same VED exposure and layer thickness as the M290. This would reveal how the part properties of the two printers differ due to only the unchangeable printer parameters (build volume, beam diameter, etc.).

V. CONCLUSION

Benchmarking using test artifacts is important for comparing and achieving similar performance between metal printers; this has implications for the scaling up of AM processes from use for initial prototyping to implementation for large scale production. This report examined physical and mechanical properties of novel test artifacts printed on EOS M100 and M290 printers using SS 316L powder. Results from 8 M290-printed and 4 M100-printed artifacts revealed no statistical difference in tensile strength, hardness, roughness, or dross formation between the printers. Tensile strengths were within EOS documented ranges of 680 to 590 MPa horizontally and 610 to 530 MPa vertically. Other observations include dross formation increasing with decreasing overhang angles, and increased burning with increasing overhang arc radii. Moving forward, material and microstructural inspections are to be completed along with prints with adjusted exposure parameters.

REFERENCES

[1] M. Schmidt, et al., “Laser based additive manufacturing in industry and academia,” CIRP Annals, vol. 66, no. 2, 2017, pp. 561-583, doi.org/10.1016/j.cirp.2017.05.011.

[2] S. Moylan, J. Slotwinski, A. Cooke, K. Jurrens, and M. A. Donmez, “Proposal for a standardized test artifact for additive manufacturing machines and processes,” Proceedings of the 2012 annual international solid freeform fabrication symposium, pp. 902-920, 2012.

[3] T. H. J. Vaneker, “The role of design for additive manufacturing in the successful economical introduction of AM,” Procedia Cirp, vol. 60, pp. 181-186, 2017.

[4] L. Gallant, A. Hsiao, and G. McSorley, “Design of a benchmark test artifact to investigate 316L stainless steel print quality and properties,” In. Proc. Canadian Society for Mechanical Engineering International Congress 2020, June 2020.

[5] J. Richter and P. Jacobs, “Accuracy,” Rapid Prototyping & Manufacturing, pp. 287-315, 1992.

[6] D. Scaravetti, P. Dubois and R. Duchamp, “Qualification of rapid prototyping tools: proposition of a procedure and a test part,” The International Journal of Advanced Manufacturing Technology, vol. 38, no. 7, pp. 683-690, 2008.

[7] E. Koc, M. Coskun, and Z. C. Oter, “Anisotropic Mechanical Behaviour of direct metal laser sintering (DMLS) parts,” unpublished.

[8] ASTM E10-15, “Standard Test Method for Brinell Hardness of Metallic Materials,” ASTM International, West Conshohocken, PA, 2015.

[9] F. Calignano, “Design optimization of supports for overhanging structures in aluminum and titanium alloys by selective laser melting,” Materials & Design, vol. 64, 2014, pp. 203-213, doi.org/10.1016/j.matdes.2014.07.043.

[10] “Design for additive metal manufacturing,” Additive Metal Manufacturing Inc., Concord, ON, Canada, 103-R23-DFMRev2, June 2016.

[11] Z. Sun, G. Vladimirov, E. Nikolaev, and L. F. Velásquez-García, “Exploration of metal 3-D printing technologies for the microfabrication of freeform, finely featured, mesoscaled structures,” Journal of Microelectromechanical Systems, vol. 27, no. 6, pp. 1171-1185, 2018.

[12] W. S. Tan, “Comparison of solid, liquid and powder forms of 3D printing techniques in membrane spacer fabrication,” Journa of Membrane Science, vol. 537, pp. 283-296, 2017.

[13] Carpenter Additive, “CT PowderRange 316L F,” datasheet, 2019.

[14] Electro Optical Systems, “EOS StainlessSteel 316L,” (EOS art.-no. 9011-0032) datasheet, 2014.

[15] Ż.A. Mierzejewska, “Effect of laser energy density, internal porosity and heat treatment on mechanical behavior of biomedical Ti6Al4V alloy obtained with DMLS technology,” Materials, vol. 12: 2331, July 2019, doi:10.3390/ma12142331.

[16] A. Guzanová, et al., “The effect of position of materials on a build platform on the hardness, roughness, and corrosion resistance of Ti6Al4V produced by DMLS technology,” Materials, vol. 9: 1055, September 2019, doi:10.3390/met9101055.

[17] B. Liu, et al., “Investigation the effect of particle size distribution on processing parameters optimisation in selective laser melting process,” International solid freeform fabrication symposium: an additive manufacturing conference. University of Texas at Austin, Austin, pp 227–238.

[18] “How to design and manufacture metal 3D-printed parts,” *protolabs.com.*

[19] D. Gu and Y. Shen, “Processing conditions and microstructural features of porous 316L stainless steel components by DMLS,” Applied Surface Science, vol. 255, no. 5, pp. 1880-1887, 2007, doi.org/10.1016/j.apsusc.2008.06.118.